

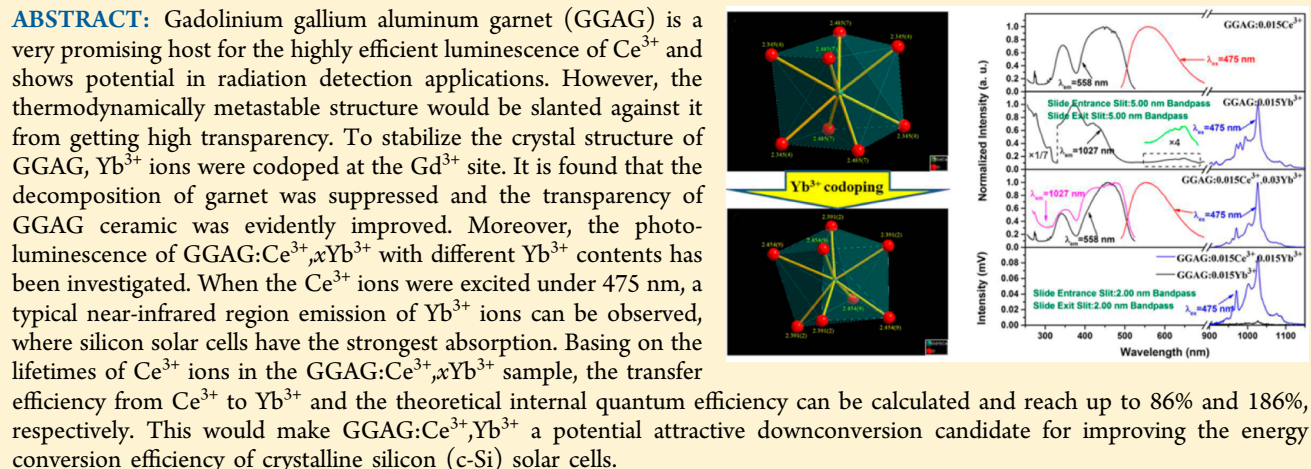
# Effect of $\text{Yb}^{3+}$ on the Crystal Structural Modification and Photoluminescence Properties of GGAG:Ce $^{3+}$

Zhao-Hua Luo,<sup>\*,†</sup> Yong-Fu Liu,<sup>†</sup> Chang-Hua Zhang,<sup>†,‡</sup> Jian-Xin Zhang,<sup>†,§</sup> Hai-Ming Qin,<sup>†</sup> Hao-Chuan Jiang,<sup>\*,†</sup> and Jun Jiang<sup>\*,†</sup>

<sup>†</sup>Ningbo Institute of Materials Technology and Engineering, Chinese Academy of Sciences, Ningbo, 315201, P. R. China

<sup>‡</sup>Department of Chemistry, College of Science, Shanghai University, Shanghai, 200444, P. R. China

<sup>§</sup>College of Electronic Information and Engineering, Hangzhou Dianzi University, Hangzhou 310018, P. R. China



## 1. INTRODUCTION

The fabrication and research of cerium doped aluminate garnets have attracted a lot of attention in recent years. The most famous compounds in this garnet family are  $\text{Y}_3\text{Al}_5\text{O}_{12}:\text{Ce}^{3+}$  (YAG:Ce $^{3+}$ ) and  $\text{Lu}_3\text{Al}_5\text{O}_{12}:\text{Ce}^{3+}$  (LuAG:Ce $^{3+}$ ). The former is one of the successful commercial phosphors for white LEDs at present, which can emit yellow light when excited by blue chips, and then the yellow light combines with the blue source to produce white light.<sup>1,2</sup> The latter is promising to be used in high energy gamma-ray detection and nuclear medical imaging as an inorganic scintillator, which mainly benefits from its satisfactory stopping power for the incident radiations, fast decay time, and high scintillation efficiency.<sup>3–5</sup> However, because of its very low natural abundance and its separation and purification being very difficult, the cost of lutetium is rather too high for industrial applications. Researchers have attempted to replace lutetium with gadolinium and form  $\text{Gd}_3\text{Al}_5\text{O}_{12}:\text{Ce}^{3+}$  (GAG:Ce $^{3+}$ ), for the reason that gadolinium's relative atomic mass is close to that of lutetium but with much lower price for its oxide. Moreover, the 4f orbits of Gd $^{3+}$  ion are half filled with electrons, and the structure of electron shell is enclosed, which makes Gd $^{3+}$  ion nonluminous and suitable as host materials. Additionally, Gd $^{3+}$  ion is a fine sensitizer for Ce $^{3+}$  ions by energy transfer, and this can enhance the luminescence efficiency of Ce $^{3+}$  ions. Unfortunately, the radius of Gd $^{3+}$  ion is 1.053 Å, larger than that of Lu $^{3+}$  ion (0.977 Å) in eight coordinate.<sup>6</sup> Some

researchers point out that the difference in ion radius makes GAG thermodynamically metastable and it would transform to orthorhombic gadolinium aluminate perovskite phase (GAP) at about 1500 °C or even lower temperature.<sup>7,8</sup> So, it seems impossible to prepare a pure-phase GAG solid material at a high temperature. The garnet structure belongs to cubic  $I\bar{a}3d$  space group, and the chemical formula of garnet can be expressed as  $\text{A}_3\text{B}_2\text{C}_3\text{O}_{12}$ , where A, B, and C represent cations occupying dodecahedral 24(c), octahedral 16(a), and tetrahedral 24(d) symmetry sites, respectively. For the ideal GAG:Ce $^{3+}$  crystal, Gd $^{3+}$  and Ce $^{3+}$  ions occupy the 24(c) sites, while 40% of Al $^{3+}$  ions take the 16(a) sites and the other 60% are located at 24(d) sites. In order to stabilize the crystal structure of GAG, ion substitution at A, B, and C sites can be used. T. Kanai et al.<sup>9</sup> have developed a new oxide scintillator  $\text{Gd}_3(\text{Al},\text{Ga})_5\text{O}_{12}:\text{Ce}^{3+}$  successfully by partially substituting Al $^{3+}$  ions with Ga $^{3+}$  ions. By Rietveld analysis, they found that the Ga $^{3+}$  ions can occupy both 16(a) and 24(d) sites. They also revealed that the GGAG:Ce scintillator exhibits excellent afterglow performance, which is crucial for medical CT applications. Later on, by systematically comparing the optical, luminescent, and scintillation characteristics of multicomponent  $(\text{Lu}_x\text{Gd}_{1-x})_3(\text{Ga}_y\text{Al}_{1-y})_5\text{O}_{12}:\text{Ce}^{3+}$  garnet single crystals, K. Kamada et al. found that the maximum light yield could

achieve almost 46,000 photons/MeV for composition of  $\text{Gd}_3\text{Al}_2\text{Ga}_3\text{O}_{12}$ .<sup>10</sup> At the same time, the energy resolution was 4.9%@662 keV and the scintillation response was quite fast.<sup>10</sup> It is generally recognized that GGAG:Ce<sup>3+</sup> compounds are promising candidates for scintillator applications.<sup>11</sup>

Although GGAG:Ce<sup>3+</sup> crystals with high quality have been grown successfully, the optical behavior of ceramics with similar compounds seems not as good, and some researchers attributed it to the moderate phase stability of GGAG.<sup>12,13</sup> In our previous work of fabricating GGAG ceramics, we observed a similar phenomenon. To modify the structure of GGAG further, rare earth ions with smaller radii compared to Gd<sup>3+</sup>, such as Y<sup>3+</sup>, Lu<sup>3+</sup>, and Tb<sup>3+</sup>, have been codoped at the Gd<sup>3+</sup> site.<sup>13–16</sup> With this compound modification, transparent ceramics GYGAG:Ce<sup>3+</sup> and GLuGAG:Ce<sup>3+</sup> exhibit excellent phase stability, and their light yield increases to 50,000–60,000 photons/MeV.<sup>12,13</sup>

Since phase stability can be achieved by partially substituting Gd<sup>3+</sup> with smaller rare earth ions, Yb<sup>3+</sup> with ion radius of 0.985 Å at dodecahedron coordination is supposed to have similar effect as Y<sup>3+</sup> and Lu<sup>3+</sup>. However, to the best of our knowledge, cerium doped YbGGAG ceramics have not been reported yet. The reason may lie in the existence of highly efficient downconversion from Ce<sup>3+</sup> to Yb<sup>3+</sup>, and this would result in luminescence quenching for Ce<sup>3+</sup> ions. On the other side, the emission wavelength of Yb<sup>3+</sup> ion (950–1100 nm) lies in the near-infrared region (NIR), where silicon solar cells have the strongest absorption.<sup>17–19</sup> Meanwhile the spectral response of crystalline silicon (c-Si) at the excitation peaks of Ce<sup>3+</sup> ions (300–500 nm) is very weak. So, the downconversion from Ce<sup>3+</sup> absorption to Yb<sup>3+</sup> emission would be a promising spectral modification approach for enhancing the efficiency of c-Si solar cells. Recently, the energy transfer between Ce<sup>3+</sup> and Yb<sup>3+</sup> has attracted a lot of interest.<sup>20–27</sup> Therefore, in the present work, we attempt to modify the phase stability of the GGAG:Ce<sup>3+</sup> ceramic by substituting Gd<sup>3+</sup> with Yb<sup>3+</sup>. The effect of Yb<sup>3+</sup> codoping on the photoluminescence behavior will also be studied.

## 2. EXPERIMENTAL SECTION

**2.1. Raw Materials and Reagents.** Rare-earth oxides such as  $\text{Gd}_2\text{O}_3$ ,  $\text{Yb}_2\text{O}_3$ , and  $\text{Ce}(\text{CO}_3)_2 \cdot 6\text{H}_2\text{O}$  with purity of 4N were purchased from Qiaodong Rare Earth Group Co., Ltd., China.  $\text{Ga}_2\text{O}_3$  with purity of 4N was provided by Chinalco. High-purity (AR, 99%)  $\text{NH}_4\text{Al}(\text{SO}_4)_2 \cdot 12\text{H}_2\text{O}$ ,  $\text{NH}_4\text{HCO}_3$ , ammonium hydroxide, nitric acid, and hydrochloric acid were purchased from Sinopharm Chemical Reagent Co., Ltd., China.

**2.2. Fabrication of GGAG:Ce<sup>3+</sup>, $x$ Yb<sup>3+</sup> Ceramics.** The starting materials were first weighed accurately according to the chemical formula of  $(\text{Ce}_{0.015}\text{Yb}_x\text{Gd}_{2.985-x})\text{Ga}_3\text{Al}_2\text{O}_{12}$  (GGAG:Ce<sup>3+</sup>, $x$ Yb<sup>3+</sup>) ( $x = 0, 0.015, 0.03, 0.09, 0.15$ , and  $0.3$ , respectively). Then, the raw material powders were dissolved in hot nitric acid and made into solution of 0.3 mol/L. After that, the resulting mixture was precipitated with ultrasonic-assisted chemical precipitation method with ammonia and ammonium carbonate mixed solution. The suspension was filtered and washed. The wet cake was dried and ground into fine powder afterward. Subsequently, the powders were calcined, molded, and sintered in oxygen atmosphere followed by hot isostatic pressing and annealing treatment. The details of powder preparation and ceramic fabrication were described in detail in our previous work.<sup>11,28</sup>

**2.3. Characterizations.** The phases of all samples were identified by an X-ray diffraction (XRD) measurement on a Bruker AXS D8 Discover diffractometer where Cu K $\alpha$  radiation ( $\lambda = 1.54056$  Å) was used. Diffraction patterns were collected in the range of 10–90° with a step scan width and scanning rate of 0.02 and 10 deg min<sup>-1</sup>. The tube

voltage and current are 40 kV and 40 mA, respectively. In addition, samples with composition of  $(\text{Ce}_{0.015}\text{Gd}_{2.985})\text{Ga}_3\text{Al}_2\text{O}_{12}$  and  $(\text{Ce}_{0.015}\text{Yb}_{0.3}\text{Gd}_{2.695})\text{Ga}_3\text{Al}_2\text{O}_{12}$  were crushed and ground into powders for further XRD measurement with the scanning rate reduced to 2.5 deg min<sup>-1</sup>. Their crystal structures were determined with Rietveld refinement by using a general structure analysis system (GSAS).<sup>29</sup> The microstructure and elementary composition of the ceramics were measured by a field emission scanning electron microscope (FEI SIRION 200) equipped with an energy-dispersive X-ray spectrometer (EDS Oxford). Room-temperature PLE, PL spectra, and fluorescence decay curves of Ce<sup>3+</sup> were measured on a Horiba FL3-111 spectrometer equipped with two different detectors for measuring visible light or near-infrared light. The visible light detector is a photomultiplier, which has a very high rate of sensitivity in the range of 270 to 700 nm. The infrared light detector is a liquid nitrogen cooled InGaAs detector, which has a high rate of sensitivity in the range of 850 to 1150 nm. Both the excitation and emission slits were set at 2–5 nm.

## 3. RESULTS AND DISCUSSION

### 3.1. Phase Characteristics and Crystalline Structure Determination.

Figure 1 presents the XRD patterns of the

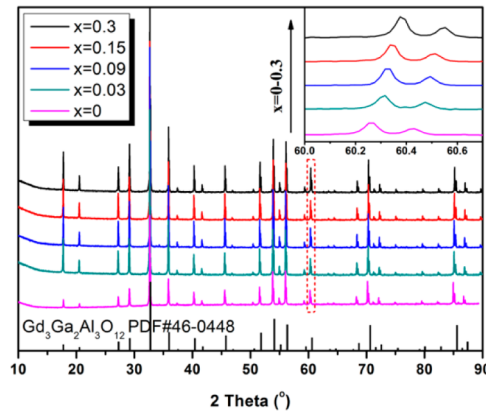
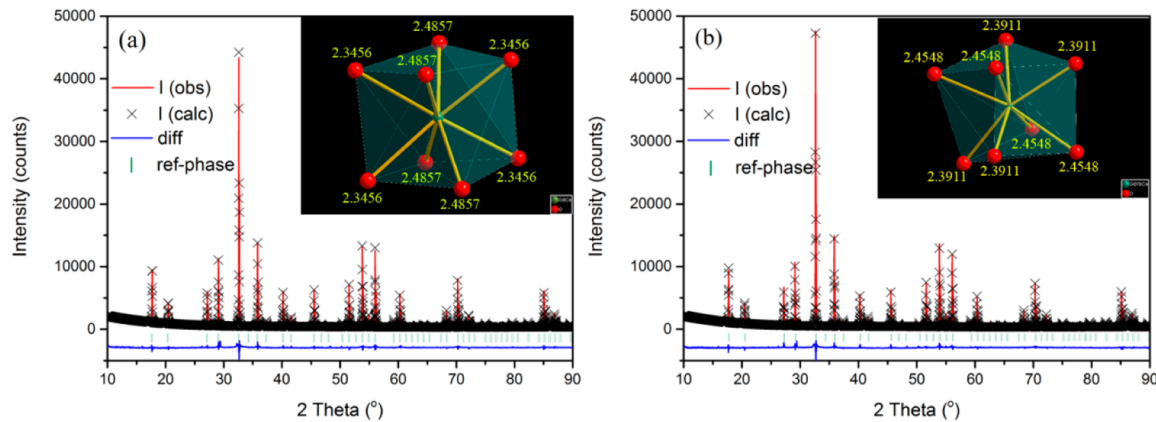


Figure 1. XRD patterns of the GGAG:Ce<sup>3+</sup>, $x$ Yb<sup>3+</sup> ( $x = 0, 0.03, 0.09, 0.15, 0.3$ ).

GGAG:Ce<sup>3+</sup>, $x$ Yb<sup>3+</sup> ( $x = 0, 0.03, 0.09, 0.15$ , and  $0.3$ , respectively) samples. The patterns show that all these samples can be assigned to a pure garnet phase according to the standard PDF # 46-0448 card. With the concentration increase of Yb<sup>3+</sup> ions, the peaks are slightly shifted toward higher angles (as seen in the inset of Figure 1), which indicates that the Yb<sup>3+</sup> ions would substitute the Gd<sup>3+</sup> sites and form a solid solution with the matrix. According to the Bragg equation, the shift of diffraction peaks reveals that the unit cell of these samples would shrink with the addition of Yb<sup>3+</sup> ions. This is because the Yb<sup>3+</sup> ionic radius ( $r = 0.985$  Å) is slightly smaller than that of Gd<sup>3+</sup> ( $r = 1.053$  Å) in an eight coordinate site, while it is ( $r = 0.868$  Å) much bigger than that of Ga<sup>3+</sup> ( $r = 0.620$  Å) or Al<sup>3+</sup> ( $r = 0.535$  Å) in a six coordinate site. Theoretically, the codoping of Yb<sup>3+</sup> ions can only take the sites of Gd<sup>3+</sup> and cause the unit cell to shrink.

To examine the structural changes of GGAG:Ce<sup>3+</sup> with the codoping of Yb<sup>3+</sup>, Rietveld refinements for GGAG:Ce<sup>3+</sup> and GGAG:Ce<sup>3+</sup>, $0.3$ Yb<sup>3+</sup> were carried out and presented in Figure 2. The crystal structural data determined with Rietveld refinements and the obtained reliability factors for GGAG:Ce<sup>3+</sup> and GGAG:Ce<sup>3+</sup>, $0.3$ Yb<sup>3+</sup> are listed in Table 1. The reliability factors in Table 1 show that the results of Rietveld refinements are reliable. From the refinement results, one can see that both



**Figure 2.** Profile fitting for GGAG:Ce<sup>3+</sup> (a) and GGAG:Ce<sup>3+</sup>, 0.3Yb<sup>3+</sup> (b) by Rietveld analysis. The insets are coordinate environments of Gd/Ce (a) and Gd/Yb/Ce (b) with oxygen atoms.

**Table 1. Crystal Data Determined with Rietveld Refinement for Ce<sub>0.015</sub>Gd<sub>2.985</sub>Ga<sub>3</sub>Al<sub>2</sub>O<sub>12</sub> (GGAG:Ce<sup>3+</sup>) and Ce<sub>0.015</sub>Yb<sub>0.3</sub>Gd<sub>2.695</sub>Ga<sub>3</sub>Al<sub>2</sub>O<sub>12</sub> (GGAG:Ce<sup>3+</sup>, 0.3Yb<sup>3+</sup>)**

formula	Ce <sub>0.015</sub> Gd <sub>2.985</sub> Ga <sub>3</sub> Al <sub>2</sub> O <sub>12</sub>	Ce <sub>0.015</sub> Yb <sub>0.3</sub> Gd <sub>2.695</sub> Ga <sub>3</sub> Al <sub>2</sub> O <sub>12</sub>
space group	Ia $\bar{3}d$	Ia $\bar{3}d$
vol (Å <sup>3</sup> )	1849.04	1844.59
unit cell dimens (Å)	$a = b = c = 12.2739$	$a = b = c = 12.2640$
Gd–O distances (Å)	$d_1 = 2.3456, d_2 = 2.4857$	$d_1 = 2.3911, d_2 = 2.4548$
structure distortion <sup>a</sup>	5.63%	2.59%
reliability factors	$R_{wp} = 8.04\%, R_p = 6.68\%, \chi^2 = 5.33$	$R_{wp} = 7.62\%, R_p = 5.91\%, \chi^2 = 7.29$

<sup>a</sup> $(d_2 - d_1)/d_2$ .

compositions belong to the  $Ia\bar{3}d$  space group with the unit cell dimensions of 12.2739 and 12.2640 Å for GGAG:Ce<sup>3+</sup> and GGAG:Ce<sup>3+</sup>, 0.3Yb<sup>3+</sup>, respectively, confirming the shrinking of the unit cell with Yb<sup>3+</sup> codoping in Figure 1. Moreover, the Gd–O bond lengths in dodecahedron-coordination unit cell are of two different values, indicating that the structure of the GdO<sub>8</sub> dodecahedron is distorted. The structure distortion for GGAG:Ce<sup>3+</sup> is 5.63%, and it is decreased to 2.59% with 10 atom % ( $x = 0.3$ ) Yb<sup>3+</sup> codoping (Table 1). This indicates that the crystal structure of GGAG becomes more stable with partial substitution of Gd by Yb. The fact that the average Gd–O distance becomes shorter in GGAG:Ce<sup>3+</sup>, 0.3Yb<sup>3+</sup> than that in GGAG:Ce<sup>3+</sup> also confirms the better stability of the crystal structure with codoping Yb<sup>3+</sup>.

Figure 3 shows the double-face polished GGAG:Ce<sup>3+</sup>,  $x$ Yb<sup>3+</sup> ( $x = 0$ –0.3) ceramics under sunlight and the 254 nm UV light,

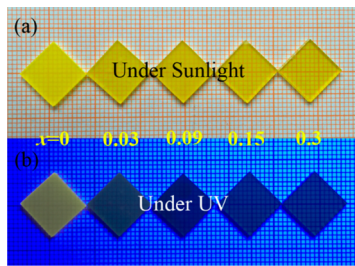


**Figure 3.** Photos of the GGAG:Ce<sup>3+</sup>,  $x$ Yb<sup>3+</sup> ( $x = 0, 0.03, 0.09, 0.15, 0.3$ ) under sunlight (a) and the 254 nm UV light (b).

respectively. It is clear that the transparency of ceramics is improved significantly with the increase of Yb<sup>3+</sup> contents. Upon taking a close look, one can find that the cloudiness (or translucency) in the GGAG:Ce<sup>3+</sup>,  $x$ Yb<sup>3+</sup> ceramics decreases gradually when  $x$  is increased from 0 to 0.15 and disappears when Yb<sup>3+</sup> content reaches 0.3.

In order to demonstrate the translucency, the microstructure of GGAG:Ce<sup>3+</sup> and GGAG:Ce<sup>3+</sup>, 0.3Yb<sup>3+</sup> ceramics was investigated and is shown in Figure 4. It appears completely

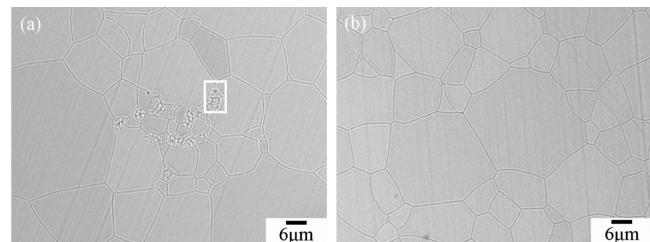


**Figure 4.** Microstructure of GGAG:Ce<sup>3+</sup> (a) and GGAG:Ce<sup>3+</sup>, 0.3Yb<sup>3+</sup> (b), respectively.

densified, and the grain sizes are almost the same for both of them. The only difference between them is that a small number of little grains with submicrometer scale exist at some grain boundary triple junctions in GGAG:Ce<sup>3+</sup> ceramics (Figure 4a). It should be noted that the amount of second phases in Figure 4a is below the detection limit of XRD, and they still show a pure garnet phase in XRD patterns (Figure 1). The EDS results for the region marked by a white box in Figure 4a exhibit composition of perovskite. According to the decomposition equation  $Gd_3Al_5O_{12} \rightarrow Al_2O_3 + 3GdAlO_3$ <sup>8,30</sup>, the perovskite phase would be the decomposition product of aluminate garnet. In addition, the grain size of the second dispersed phase is much smaller than that of the garnet matrix, which means that their sintering characteristics are different from those of garnet. Therefore, it is reasonable to believe that the second dispersed phase in Figure 4a is perovskite phase, and it would result in the translucency in GGAG:Ce<sup>3+</sup> ceramics due to scattering caused by the refraction index mismatch. The absence of a second dispersed phase in GGAG:Ce<sup>3+</sup>, 0.3Yb<sup>3+</sup> samples indicates that the codoping of 10 atom % Yb<sup>3+</sup> ions ( $x = 0.3$ ) in Gd<sup>3+</sup> sites is able to fully stabilize GGAG:Ce<sup>3+</sup> crystalline structure.

### 3.2. Luminescence of Yb<sup>3+</sup> Codoped GGAG:Ce<sup>3+</sup> Ceramics.

Figure 5a–c presents the normalized PLE and PL

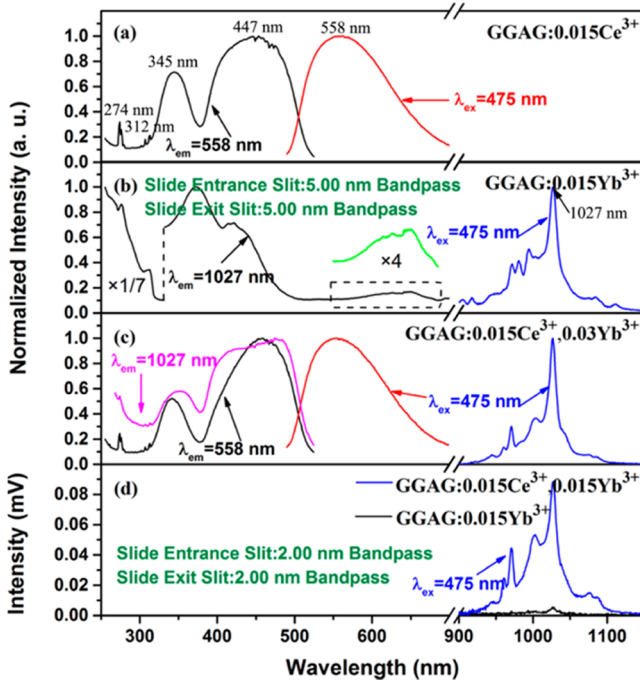


Figure 5. Normalized PLE and PL spectra of GGAG:0.015Ce<sup>3+</sup> (a), GGAG:0.015Yb<sup>3+</sup> (b), and GGAG:0.015Ce<sup>3+</sup>, 0.03Yb<sup>3+</sup> (c) and the PL spectra of GGAG:0.015Ce<sup>3+</sup>, 0.015Yb<sup>3+</sup> and GGAG:0.015Yb<sup>3+</sup> (d).

spectra of Ce<sup>3+</sup> singly doped, Yb<sup>3+</sup> singly doped, and Ce<sup>3+</sup>–Yb<sup>3+</sup> codoped GGAG ceramics, respectively. In addition, the PL spectra of GGAG:0.015Ce<sup>3+</sup>, 0.015Yb<sup>3+</sup> and GGAG:0.015Yb<sup>3+</sup> are shown in Figure 5d. The side entrance and exit slits were set to 2 nm in Figure 5a,c,d, while they were set to 5 nm in Figure 5b. It should be noted that two different detectors were used in visible and near-infrared light ranges, so the units of the ordinate are different. The PLE spectrum of the Ce<sup>3+</sup> singly doped GGAG consists of two strong broad and two weak sharp excitation bands peaking at 447, 345, 312, and 274 nm, and they are related to the 4f–5d<sub>1</sub> and 4f–5d<sub>2</sub> transitions of Ce<sup>3+</sup> ions and the <sup>8</sup>S<sub>7/2</sub>–<sup>6</sup>P<sub>7/2</sub> and <sup>8</sup>S<sub>7/2</sub>–<sup>6</sup>I<sub>7/2</sub> transitions of Gd<sup>3+</sup> ions, respectively (Figure 5). Under the 475 nm excitation, a typical emission band of Ce<sup>3+</sup> ions peaking at around 558 nm arises. For PLE spectrum of Yb<sup>3+</sup> singly doped GGAG, the <sup>8</sup>S<sub>7/2</sub>–<sup>6</sup>P<sub>7/2</sub> and <sup>8</sup>S<sub>7/2</sub>–<sup>6</sup>I<sub>7/2</sub> transitions of Gd<sup>3+</sup> ions are clearly observed by monitoring the <sup>2</sup>F<sub>5/2</sub>–<sup>2</sup>F<sub>7/2</sub> transition of Yb<sup>3+</sup> at 1027 nm (Figure 5b), which illustrates that there is strong energy transfer from Gd<sup>3+</sup> to Yb<sup>3+</sup>. The excitation bands ranging from 330 to 500 nm and from 580 to 680 nm would be related to localized exciton transitions, which would be caused by structure defects.<sup>31</sup> Moreover, the excitation band from 580 to 680 nm overlaps with the Ce<sup>3+</sup> emission band, indicating that energy transfers from Ce<sup>3+</sup> to Yb<sup>3+</sup> can take place upon the Ce<sup>3+</sup> excitation. When excited under 475 nm, a typical NIR emission band of Yb<sup>3+</sup> ions appears. It should be noted that the excitation spectrum of Yb<sup>3+</sup> singly doped GGAG in Figure 5b overlaps with that of Ce<sup>3+</sup> singly doped ones in Figure 5a. In order to identify the main source of energy for emission of Yb<sup>3+</sup> ions, the absolute NIR emission intensities of GGAG:0.015Ce<sup>3+</sup>, 0.015Yb<sup>3+</sup> and GGAG:0.015Yb<sup>3+</sup> are compared in Figure 5d. It is noticeable that the emission intensity of Ce<sup>3+</sup> and Yb<sup>3+</sup> codoped GGAG is much stronger than that with Yb<sup>3+</sup> singly doped ones, which indicates that the main source of energy for emission of Yb<sup>3+</sup> ions comes from Ce<sup>3+</sup> rather than the

structure defects. In Ce<sup>3+</sup> and Yb<sup>3+</sup> codoped GGAG, the PLE spectra appear similar whether by monitoring the 5d–4f transition of Ce<sup>3+</sup> at 558 nm or the <sup>2</sup>F<sub>5/2</sub>–<sup>2</sup>F<sub>7/2</sub> transition of Yb<sup>3+</sup> at 1027 nm (Figure 5c). Meanwhile, the PL spectra exhibit both strong Ce<sup>3+</sup> emission at 558 nm and Yb<sup>3+</sup> emission at 1027 nm, verifying the existence of energy transfers from Ce<sup>3+</sup> to Yb<sup>3+</sup>.

The visible and NIR PL spectra of GGAG:Ce<sup>3+</sup>, *x*Yb<sup>3+</sup> (*x* = 0–0.3) under 475 nm excitation is presented in Figure 6a and

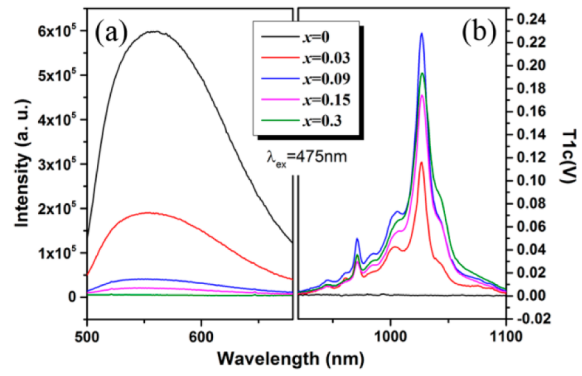
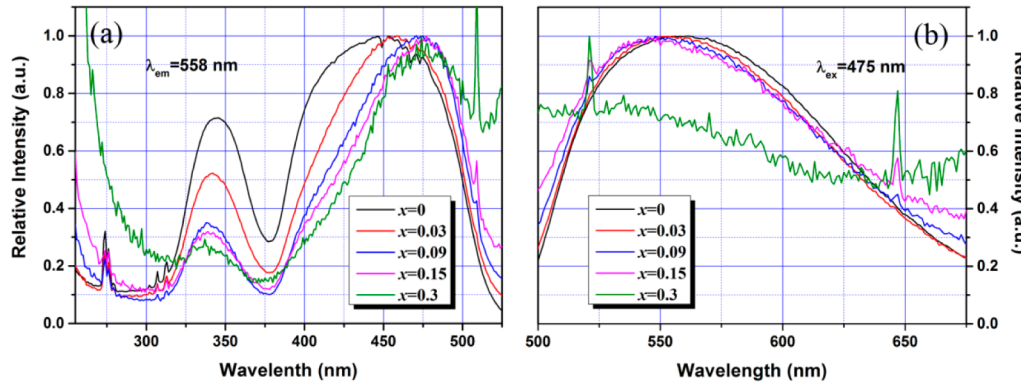


Figure 6. Visible (a) and NIR (b) PL spectra of GGAG:Ce<sup>3+</sup>, *x*Yb<sup>3+</sup> (*x* = 0, 0.03, 0.09, 0.15, 0.3) under the 475 nm excitation.

Figure 6b, respectively. Obviously, as the amount of Yb<sup>3+</sup> ions increases from 0 to 0.3, the emission intensity of Ce<sup>3+</sup> centered at 558 nm declines dramatically (Figure 6a). This trend can be intuitively seen from the light and shade degree of samples under 254 nm UV light, which is presented in Figure 3b. Meanwhile, the luminescence of Yb<sup>3+</sup> first reaches a maximum when the Yb<sup>3+</sup> concentration reaches *x* = 0.09 (3 atom % at the Gd site), and then it decreases with further Yb<sup>3+</sup> addition (Figure 6b). We noted that the optimal Yb<sup>3+</sup> concentration in this study is lower than that in other reported systems.<sup>18,26</sup> The reason could be related to the relatively low Ce<sup>3+</sup> concentration in this research, rather than the Yb<sup>3+</sup> concentration quenching.<sup>32</sup> The emission intensity changes of Ce<sup>3+</sup> and Yb<sup>3+</sup> over various *x* values confirm the energy transfer from Ce<sup>3+</sup> to Yb<sup>3+</sup> in GGAG ceramics.

The normalized concentration-dependent PLE and PL spectra for GGAG:Ce<sup>3+</sup>, *x*Yb<sup>3+</sup> with *x* varying from 0 to 0.3 are presented in Figure 7. The PLE spectra were monitored at the emission maximum wavelength of Ce<sup>3+</sup> around 558 nm, and the PL spectra were recorded under the 475 nm excitation. With the increase of Yb<sup>3+</sup> contents, the excitation peaks around 274 and 312 nm for the 4f–4f transition of Gd<sup>3+</sup> ion do not change, whereas the excitation peaks at 345 and 447 nm are shifted to shorter and longer wavelengths, respectively (Figure 7a). The blue and red shifts indicate that the lowest excited Sd<sub>1</sub> state energy level of Ce<sup>3+</sup> ions shifts to an even lower energy position, while the Sd<sub>2</sub> level shifts in an opposite way. P. Dorenbos pointed out that the main crystal-field splitting 10D<sub>q</sub> is a quite normally observed value for Ce<sup>3+</sup> in cubical coordination, and the type of host rare earth cation chosen affects additional  $\Delta_{12}$  splitting between the first two [LS] 5d levels for Ce<sup>3+</sup> but not 10D<sub>q</sub> in garnet.<sup>33</sup> In general, the reason for the increase of energy separation between Sd<sub>1</sub> and Sd<sub>2</sub> levels lies in the enlargement of the  $\Delta_{12}$  splitting caused by the enhancement of crystal field strength. However, according to the results of Rietveld refinement as shown in Table 1, the structure distortion of GdO<sub>8</sub> dodecahedron has been improved



**Figure 7.** Concentration-dependent normalized PLE monitored at 558 nm (the emission maximum wavelength of  $\text{Ce}^{3+}$ ) (a) and PL under 475 nm excitation (b) spectra for GGAG:Ce $^{3+}$ , $x$ Yb $^{3+}$  ( $x = 0\text{--}0.3$ ) ceramics.

a little and the average Gd–O distance extends a little, meaning that the  $\Delta_{12}$  splitting of Ce $^{3+}$  should be decreased. So, the crystal field change would not be the main cause of the shift of excitation peaks in Figure 7a. From Figure 5b, we can see that there is a strong localized exciton transition between 330 and 500 nm, which can excite the luminescence of Yb $^{3+}$  ions. Accordingly, this part of energy for Ce $^{3+}$  excitation will decrease with codoping of Yb $^{3+}$ , and this may be the main reason for the shift of excitation peaks at 345 and 447 nm. Moreover, a slight “blue shift” phenomenon occurs in emission spectra at higher Yb $^{3+}$  concentrations (Figure 7b), which seems contradictory to the “red shift” in Figure 7a. It can be mainly attributed to two factors. One is the enhancement of GdO<sub>8</sub> dodecahedron symmetry as mentioned above, and the other is structure defects. It is well-known that the PL spectrum of Ce $^{3+}$  can be decomposed into two emission bands, namely 5d– $2\text{F}_{5/2}$  and 5d– $2\text{F}_{7/2}$ . From Figure 4b, we can also know that there is an excitation band ranging from 580 to 680 nm, overlapping with the 5d– $2\text{F}_{5/2}$  emission portions, which means that this part of energy can be transferred to Yb $^{3+}$  ions. Consequently, the percentage of the 5d– $2\text{F}_{5/2}$  emission portion declines and it results in the apparent phenomenon of “blue shift”. Besides the main emission band of Ce $^{3+}$ , two narrow peaks around 521 and 647 nm emerge when the Yb $^{3+}$  content exceeds 0.09 (Figure 7b). These two narrow emission peaks are attributed to the  $2\text{H}_{11/2}$ – $4\text{I}_{15/2}$  and  $4\text{F}_{9/2}$ – $4\text{I}_{15/2}$  transitions of impurity Er $^{3+}$  ions, respectively.<sup>34</sup> Moreover, the emission intensity of Er $^{3+}$  shows an upward trend with increasing Yb $^{3+}$  content, which is due to the energy transfer from Yb $^{3+}$  to Er $^{3+}$ .<sup>35,36</sup> Because it is not the issue we are concerned with in this study, and the Er $^{3+}$  has very little impact on the emission of Yb $^{3+}$  and Ce $^{3+}$ , the luminescence characteristics of Er $^{3+}$  will not be discussed in detail.

The energy level schematic diagrams of Gd $^{3+}$ , Ce $^{3+}$ , Yb $^{3+}$ , and Er $^{3+}$  ions based on the PLE and PL spectra are shown in Figure 8 along with the proposed energy transfer mechanism in the GGAG host. There are four possible ET routes among Gd $^{3+}$ , Ce $^{3+}$ , Yb $^{3+}$ , and the impurity Er $^{3+}$  ions in GGAG. When the Gd $^{3+}$  ions are excited from the  $2\text{S}_{7/2}$  level to  $2\text{P}_{7/2}$  or  $2\text{I}_{7/2}$  levels, their energy can transfer to the nearby Ce $^{3+}$  and Yb $^{3+}$  ions. Then, the 5d $_1$  state of Ce $^{3+}$  will be populated through fast nonradiative relaxation from the 5d $_2$  state and leads to the emission of Ce $^{3+}$  at around 558 nm. At the same time, part of the excited energy would transfer to one or two Yb $^{3+}$  ions, resulting in the NIR emission of Yb $^{3+}$  ions at around 1027 nm. Additionally, upconversion emissions of Er $^{3+}$  ions will also take

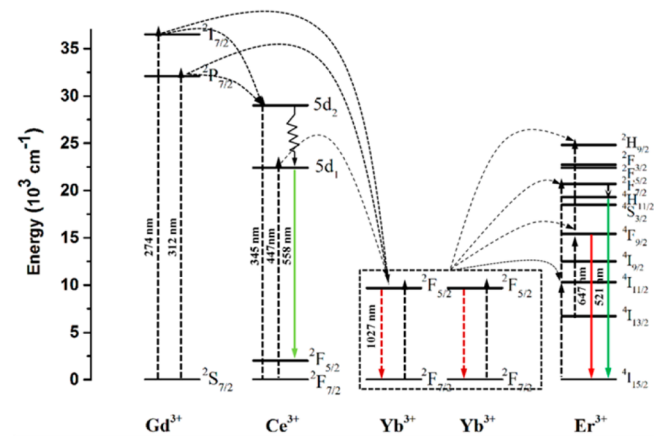


**Figure 8.** Energy level schematic diagrams of Gd $^{3+}$ , Ce $^{3+}$ , Yb $^{3+}$ , and Er $^{3+}$  ions, and possible processes of populations and emissions.

place due to the phonon-assisted energy transfer from Yb $^{3+}$  to Er $^{3+}$ .

In order to investigate the cooperative energy transfer (CET) efficiency in GGAG:Ce $^{3+}$ , $x$ Yb $^{3+}$  ( $x = 0\text{--}0.3$ ), the decay curves of the 5d $_1$ –4f transition for Ce $^{3+}$  ( $\lambda_{\text{em}} = 558$  nm) have been measured under the 458 nm excitation (Figure 9). Meanwhile,

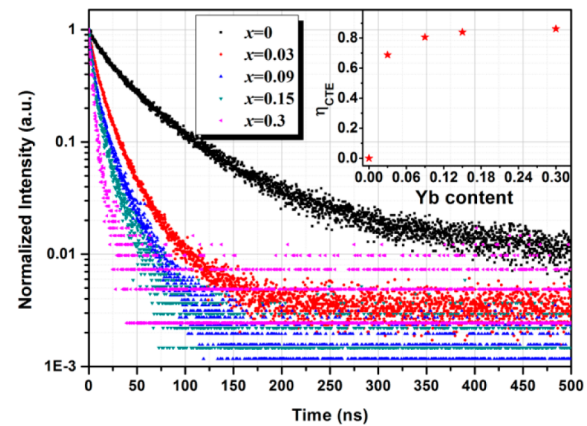


**Figure 9.** Normalized photoluminescence decay curves of the Ce $^{3+}$ :5d $_1$ –4f transition under 458 nm excitation in GGAG:Ce $^{3+}$ , $x$ Yb $^{3+}$  ( $x = 0\text{--}0.3$ ). The inset is the  $\eta_{\text{CET}}$  with different Yb doping concentrations.

the CET efficiencies ( $\eta_{\text{CET}}$ ) are plotted in the inset of Figure 9. The  $\eta_{\text{CET}}$  is determined with the following equation:<sup>32,37</sup>

$$\eta_{\text{CET},x\text{Yb}} = 1 - \frac{\tau_{x\text{Yb}}}{\tau_0} \quad (1)$$

where the  $\tau_{x\text{Yb}}$  and  $\tau_0$  are the lifetimes of samples with and without  $\text{Yb}^{3+}$ , respectively. Since the decay curves exhibit a slight nonexponentiality, average lifetimes are used in eq 1, which can be formulated by<sup>38</sup>

$$\tau_{x\text{Yb}} = \int_0^\infty I_x(t) dt \quad (2)$$

where  $I_x(t)$  stands for the normalized fluorescence intensity at time  $t$  with the  $\text{Yb}^{3+}$  content  $x$  varying from 0 to 0.3. Basing on the results of integration, it can be found that the average decay times of  $\text{Ce}^{3+}$  decrease from 50.4 to 6.9 ns with the  $\text{Yb}^{3+}$  content increasing from 0 to 0.3, which offers compelling evidence for the energy transfer from  $\text{Ce}^{3+}$  to  $\text{Yb}^{3+}$ . In addition, as is illustrated in the inset of Figure 9, the CET efficiency  $\eta_{\text{CET}}$  increases dramatically at first when the content of  $\text{Yb}^{3+}$  is lower than 0.09, and then it increases slowly and reaches 86% for  $x = 0.3$ . The theoretical internal quantum efficiency  $\eta_{\text{QE}}$  can be calculated according to<sup>32</sup>

$$\eta_{\text{QE}} = \eta_{\text{Ce}}(1 - \eta_{\text{CET}}) + 2\eta_{\text{Yb}}\eta_{\text{CET}} \quad (3)$$

where  $\eta_{\text{Ce}}$  and  $\eta_{\text{Yb}}$  denote the luminescent quantum efficiencies of  $\text{Ce}^{3+}$  and  $\text{Yb}^{3+}$ , respectively. Assuming the value of  $\eta_{\text{Ce}}$  and  $\eta_{\text{Yb}}$  to be 1, an  $\eta_{\text{QE}}$  of 186% can be obtained with the  $\text{Yb}^{3+}$  content  $x = 0.3$  (10 atom %), which is higher than the QEs (48%–174%) in other  $\text{Ce}^{3+}$  and  $\text{Yb}^{3+}$  codoped hosts.<sup>18,21,24</sup> Furthermore, it is important to point out that there are two other factors that should not be neglected for the practical application of GGAG:Ce<sup>3+</sup>,Yb<sup>3+</sup>. One factor is the perfect match of  $\text{Yb}^{3+}$  emission and the optimum spectral response of c-Si. The other factor is that the excitation spectrum of  $\text{Ce}^{3+}$  locates in a range of low spectral response of c-Si but matches well with the solar spectrum. So, there is reason to believe that the Ce<sup>3+</sup>–Yb<sup>3+</sup> codoped GGAG transparent ceramics hold great application promise for improving the conversion efficiency of c-Si solar cells.

#### 4. CONCLUSION

Cerium doped gadolinium gallium aluminum garnet (GGAG:Ce<sup>3+</sup>) transparent ceramic shows potential in high energy particle detection applications. However, the thermodynamically metastable structure would be slanted against it from getting high transparency. On the basis of Rietveld refinement, we found that the structures of  $\text{GdO}_8$  dodecahedron were distorted. With partial substitution of  $\text{Yb}^{3+}$  at the  $\text{Gd}^{3+}$  site, the polyhedral distortion was corrected slightly, implying that the crystal structure became more stable. Consequently, the decomposition of garnet could be suppressed and the transparency of GGAG ceramic was evidently improved. Moreover, the photoluminescence of GGAG:Ce<sup>3+</sup>, $x\text{Yb}^{3+}$  with different  $\text{Yb}^{3+}$  contents has been investigated. In comparison of the excitation and emission spectra of  $\text{Ce}^{3+}$  and  $\text{Yb}^{3+}$  singly doped and  $\text{Ce}^{3+}$ – $\text{Yb}^{3+}$  codoped GGAG, efficient energy transfer from  $\text{Ce}^{3+}$  to  $\text{Yb}^{3+}$  was observed in this host. The transfer efficiency reached up to 86% based on the measured  $\text{Ce}^{3+}$  lifetimes in the GGAG:Ce<sup>3+</sup>, $x\text{Yb}^{3+}$  sample. This can be a potential attractive downconversion candidate for

improving the energy conversion efficiency of crystalline silicon (c-Si) solar cells.

#### ■ AUTHOR INFORMATION

##### Corresponding Authors

\*E-mail: luozhaohua@nimte.ac.cn. Tel: 86-574-87913381. Fax: 86-574-86382329. No. 1219 Western Zhongguan Road, Ningbo 315201, China. (Z.-H.L.).

\*E-mail: jianghaochuan@nimte.ac.cn (H.-C.J.).

\*E-mail: jjun@nimte.ac.cn (J.J.).

##### Notes

The authors declare no competing financial interest.

#### ■ ACKNOWLEDGMENTS

This work is financially supported by the National Natural Science Foundation of China (NSFC51402317, 11404351, 51502308) and Public Projects of Zhejiang Province (2015C33104).

#### ■ REFERENCES

- (1) Nakamura, S. *Science* **1998**, *281*, 956–961.
- (2) Denault, K. A.; Brégoch, J.; Gaultois, M. W.; Mikhailovsky, A.; Petry, R.; Winkler, H.; DenBaars, S. P.; Seshadri, R. *Chem. Mater.* **2014**, *26*, 2275–2282.
- (3) Dujardin, C.; Mancini, C.; Amans, D.; Ledoux, G.; Abler, D.; Auffray, E.; Lecoq, P.; Perrodin, D.; Petrosyan, A.; Ovanesyan, K. L. *J. Appl. Phys.* **2010**, *108*, 013510.
- (4) Nikl, M.; Yoshikawa, A. *Adv. Opt. Mater.* **2015**, *3*, 463–481.
- (5) Nikl, M.; Kamada, K.; Babin, V.; Pejchal, J.; Pilarova, K.; Mihokova, E.; Bejtlerova, A.; Bartosiewicz, K.; Kurosawa, S.; Yoshikawa, A. *Cryst. Growth Des.* **2014**, *14*, 4827–4833.
- (6) Shannon, R. D. *Acta Crystallogr., Sect. A: Cryst. Phys., Diffraction, Theor. Gen. Crystallogr.* **1976**, *32*, 751–767.
- (7) Chiang, C.-C.; Tsai, M.-S.; Hon, M.-H. *J. Electrochem. Soc.* **2007**, *154*, J326–J329.
- (8) Li, J.; Li, J.-G.; Zhang, Z.; Wu, X.; Liu, S.; Li, X.; Sun, X.; Sakka, Y. *J. Am. Ceram. Soc.* **2012**, *95*, 931–936.
- (9) Kanai, T.; Satoh, M.; Miura, I. *J. Am. Ceram. Soc.* **2008**, *91*, 456–462.
- (10) Kamada, K.; Yanagida, T.; Endo, T.; Tsutumi, K.; Usuki, Y.; Nikl, M.; Fujimoto, Y.; Fukabori, A.; Yoshikawa, A. *J. Cryst. Growth* **2012**, *352*, 88–90.
- (11) Luo, Z.; Jiang, H.; Jiang, J.; Mao, R. *Ceram. Int.* **2015**, *41*, 873–876.
- (12) Wang, Y.; Baldoni, G.; Rhodes, W. H.; Brecher, C.; Shah, A.; Shirwadkar, U.; Glodo, J.; Cherepy, N.; Payne, S. *Proc. SPIE* **2012**, *8507*, 850717.
- (13) Cherepy, N. J.; Seeley, Z. M.; Payne, S. A.; Beck, P. R.; Swanberg, E. L.; Hunter, S.; Ahle, L.; Fisher, S. E.; Melcher, C.; Wei, H.; Stefanik, T.; Chung, Y. S.; Kindem, J. *Proc. SPIE* **2014**, *9213*, 921302.
- (14) Chewpraditkul, W.; Panek, D.; Bruza, P.; Chewpraditkul, W.; Wanarak, C.; Pattanaboonmee, N.; Babin, V.; Bartosiewicz, K.; Kamada, K.; Yoshikawa, A.; Nikl, M. *J. Appl. Phys.* **2014**, *116*, 083505.
- (15) Cherepy, N. J.; Seeley, Z. M.; Payne, S. A.; Beck, P. R.; Drury, O. B.; O’Neal, S. P.; Figueiroa, K. M.; Hunter, S.; Ahle, L.; Thelin, P. A.; Stefanik, T.; Kindem, J. *IEEE Trans. Nucl. Sci.* **2013**, *60*, 2330–2335.
- (16) Wu, Y.; Ren, G. *CrystEngComm* **2013**, *15*, 4153–4161.
- (17) Liu, Z.; Li, J.; Yang, L.; Chen, Q.; Chu, Y.; Dai, N. *Sol. Energy Mater. Sol. Cells* **2014**, *122*, 46–50.
- (18) Li, J.; Chen, L.; Hao, Z.; Zhang, X.; Zhang, L.; Luo, Y.; Zhang, J. *Inorg. Chem.* **2015**, *54*, 4806–4810.
- (19) Richards, B. S. *Sol. Energy Mater. Sol. Cells* **2006**, *90*, 2329–2337.
- (20) Sontakke, A. D.; Ueda, J.; Katayama, Y.; Dorenbos, P.; Tanabe, S. *Appl. Phys. Lett.* **2015**, *106*, 131906.

(21) Fang, Z.; Cao, R.; Zhang, F.; Ma, Z.; Dong, G.; Qiu, J. *J. Mater. Chem. C* **2014**, *2*, 2204–2211.

(22) Ueda, J.; Tanabe, S. *J. Appl. Phys.* **2009**, *106*, 043101.

(23) Sontakke, A. D.; Ueda, J.; Katayama, Y.; Zhuang, Y.; Dorenbos, P.; Tanabe, S. *J. Appl. Phys.* **2015**, *117*, 013105.

(24) Chen, D.; Wang, Y.; Yu, Y.; Huang, P.; Weng, F. *J. Appl. Phys.* **2008**, *104*, 116105.

(25) Boccolini, A.; Marques-Hueso, J.; Chen, D.; Wang, Y.; Richards, B. S. *Sol. Energy Mater. Sol. Cells* **2014**, *122*, 8–14.

(26) Yu, D. C.; Rabouw, F. T.; Boon, W. Q.; Kieboom, T.; Ye, S.; Zhang, Q. Y.; Meijerink, A. *Phys. Rev. B: Condens. Matter Mater. Phys.* **2014**, *90*, 165126.

(27) You, F.; Bos, A. J. J.; Shi, Q.; Huang, S.; Dorenbos, P. *J. Phys.: Condens. Matter* **2011**, *23*, 215502.

(28) Luo, Z.; Jiang, H.; Jiang, J. *J. Am. Ceram. Soc.* **2013**, *96*, 3038–3041.

(29) Larson, A. C.; Dreele, R. B. V. *General structure analysis system (GSAS)*; Los Alamos National Laboratory Report: LA–UR: 2000; pp 86–748.

(30) Li, J.-G.; Sakka, Y. *Sci. Technol. Adv. Mater.* **2015**, *16*, 014902.

(31) Luo, J.; Wu, Y.; Zhang, G.; Zhang, H.; Ren, G. *Opt. Mater.* **2013**, *36*, 476–481.

(32) Vergeer, P.; Vlugt, T.; Kox, M.; den Hertog, M.; van der Eerden, J.; Meijerink, A. *Phys. Rev. B: Condens. Matter Mater. Phys.* **2005**, *71*, 014119.

(33) Dorenbos, P. *J. Lumin.* **2013**, *134*, 310–318.

(34) Zhai, X.; Li, J.; Liu, S.; Liu, X.; Zhao, D.; Wang, F.; Zhang, D.; Qin, G.; Qin, W. *Opt. Mater. Express* **2013**, *3*, 270–277.

(35) Wang, F.; Liu, X. *J. Am. Chem. Soc.* **2008**, *130*, 5642–5643.

(36) Wang, F.; Liu, X. *Chem. Soc. Rev.* **2009**, *38*, 976–989.

(37) Zhang, Q. Y.; Yang, C. H.; Pan, Y. X. *Appl. Phys. Lett.* **2007**, *90*, 021107.

(38) Liu, Y.; Zhang, X.; Hao, Z.; Luo, Y.; Wang, X.; Zhang, J. *J. Mater. Chem.* **2011**, *21*, 16379–16384.